applied sciences

MDPI

Article

Annual Acceptable Collapse Probability and CMR of Viscous-Damped Structures Considering Seismic Hazard and Total Uncertainty

Xi Zhao [1,2,3] and Wen Pan [1,3,*]

[1] Faculty of Civil Engineering and Mechanics, Kunming University of Science and Technology, Kunming 650500, China; 2015058@ynau.edu.cn
[2] College of Water Conservancy, Yunnan Agricultural University, Kunming 650201, China
[3] Yunnan Earthquake Engineering Technology Research Center, Kunming 650500, China
* Correspondence: wenpan@kust.edu.cn

Abstract

Seismic collapse can cause catastrophic losses, and acceptable annual collapse probability with its CMR target is a core metric in performance-based design. Existing ATC-63-based CMR research mainly addresses non-damped systems and often uses a single lumped dispersion, obscuring damper-reliability contributions and hindering alignment with CECS 392 limits. This study proposes a unified, code-consistent decision framework for acceptable annual collapse probability and CMR that jointly accounts for seismic hazard and damper-related uncertainty. The total collapse dispersion is decomposed as $\sigma^2_{\text{total,damp}} = \sigma^2_{\text{base}} + \sigma^2_{\text{damper}}$, where σ_{base} represents background dispersion independent of dampers and σ_{damper} captures incremental uncertainty induced by degradation and partial failure. A code-designed viscous-damped RC frame is evaluated under three scenarios (nominal damping, 20% damping-coefficient reduction, and 7% random damper failures). Using the same 14 records and $\text{Sa}(T_1, 5\%)$ as the intensity measure, multi-stripe IDA and Probit-based lognormal fragility fitting yield median collapse intensities $\text{Sc} \approx 2.18 - 2.24$ g, with only ~2–3% reduction under mild degradation/failure. A random-effects variance decomposition identifies $\sigma_{\text{damper}} \approx 0$, indicating a limited marginal contribution of damper-related uncertainty within the degradation range considered in this study. Closed-form relationships between annual collapse rate, Sc, and $\sigma_{\text{total,damp}}$ are then derived under a power-law hazard model and inverted to generate acceptable-risk intervals and CMR target curves/matrices. Results show that higher design intensity and larger $\sigma_{\text{total,damp}}$ demand substantially higher CMR, highlighting potential risk underestimation when relying solely on nominal CMR. The framework enables explicit identification of damper-related uncertainty from limited collapse data and provides a practical workflow for collapse-prevention design and post-assessment under explicitly defined scenario conditions, with a clear pathway for extension to broader scenario spaces.

Keywords: viscous damping; collapse uncertainty; annual collapse probability; collapse margin ratio (CMR); random-effects model

Check for updates

Academic Editors: Lianxu Zhou and Aijun Ye

Received: 10 February 2026
Revised: 22 March 2026
Accepted: 25 March 2026
Published: 29 March 2026

Copyright: © 2026 by the authors. Licensee MDPI, Basel, Switzerland. This article is an open access article distributed under the terms and conditions of the Creative Commons Attribution (CC BY) license.

1. Introduction

Global collapse under extreme earthquakes is one of the most catastrophic structural failure modes, resulting in severe casualties and considerable economic losses. To control

collapse risk, buildings should retain sufficient collapse-prevention safety margins throughout their design life, so that collapse probabilities remain within socially acceptable limits even under earthquakes exceeding the design-basis level. Therefore, it is necessary to define acceptable collapse probabilities and establish graded ranges for buildings with different importance categories. These ranges should be further formulated into computable and comparable quantitative indicators for use in collapse-prevention design and assessment. Such a framework supports risk-informed decision making and facilitates the development of practical collapse-prevention design approaches.

In recent years, supplemental energy-dissipation technologies, particularly viscous dampers, have been widely implemented in important buildings located in high-seismic-intensity regions and in the seismic retrofit of existing structures. By providing additional damping and energy dissipation, these devices reduce structural demands under earthquake excitation. As a result, the collapse margin under strong ground motions can be increased and the collapse risk becomes more controllable. Current practice for damped structures is largely framed around response-control indices, such as damper energy-dissipation efficiency, interstory drift ratio, and floor acceleration. The primary focus is to satisfy serviceability requirements and component-level damage objectives [1].

However, for viscous-damped structures, it remains unclear what minimum collapse-prevention safety margin should be achieved under the same design intensity. It is also unclear whether the overall collapse risk can be materially reduced once uncertainties from damper parameter variability, in-service degradation, and potential partial failures are explicitly considered. A unified and quantifiable decision criterion is still lacking [2]. In engineering applications, damping devices may sometimes substitute for part of conventional seismic detailing (e.g., modest reductions in reinforcement or member sizes). Without verification constraints directly linked to collapse reliability, reduced response demands may mask an implicit loss of safety redundancy at the ultimate limit state [3]. Therefore, damping benefits and damper-uncertainty costs should be evaluated within a consistent metric. This is necessary to define the minimum required collapse-prevention safety margin for damped structures at a given design intensity [4].

The collapse margin ratio (CMR) is one of the most widely used safety-margin indices in international collapse assessment. It is defined as the ratio between the median collapse intensity (at 50% collapse probability) and the code-specified "maximum considered earthquake" intensity. It reflects the collapse-prevention redundancy relative to code demand [5]. CMR is physically intuitive, follows a standardized calculation procedure, and supports consistent comparisons across design alternatives. It has therefore become a key quantitative descriptor in collapse-performance studies [6–8].

Based on CMR, the FEMA P695/ATC-63 methodology provides a mature evaluation procedure. Collapse fragility curves are developed using incremental dynamic analysis (IDA). CMR or the adjusted CMR (ACMR) is then computed and used to compare collapse safety margins across structural systems and design schemes [9–11]. However, most existing applications focus on relative comparisons. A risk-consistent quantitative definition of an "acceptable threshold" required to meet collapse-prevention objectives remains limited. Moreover, using fixed CMR/ACMR acceptance values in design decisions has two inherent limitations. First, the threshold is tied to a specific hazard definition and target risk level. Its implied risk meaning may change when code provisions, hazard levels, or societal risk objectives are updated [12]. Second, CMR does not explicitly account for site-specific hazard. When hazard curves vary with region, site class, or design intensity, the same CMR can correspond to different lifetime collapse probabilities. This weakens risk comparability across regions and engineering conditions [13].

The annual collapse probability (or annual collapse rate) obtained by convolving site-specific seismic hazard with collapse fragility directly links collapse capacity to regional hazard. It provides a risk metric with a clear probabilistic meaning and enables consistent comparisons across regions and building importance categories [14]. Acceptable collapse safety-margin thresholds back-calculated from this metric can avoid the risk bias that may arise when fixed CMR limits are applied under different hazard conditions.

In hazard–fragility coupling, collapse uncertainty directly governs the dispersion of the fragility curve. It therefore controls the annual collapse rate associated with a given median collapse intensity. For a fixed risk target, larger uncertainty requires a higher median collapse capacity and a higher acceptable CMR [5]. Existing studies and the FEMA P695 procedure typically combine record-to-record variability, modeling assumptions, detailing effects, and test-related errors into a single total dispersion parameter [5,15]. This treatment is reasonable for conventional lateral-force-resisting systems. However, it may not capture uncertainty effects specific to viscous-damped structures. Damper effectiveness depends on multiple factors, including damping coefficient, velocity exponent, capacity, and installation/connection quality. Manufacturing variability, environmental effects and in-service degradation, construction deviations, and partial failures can introduce systematic shifts in median collapse capacity across damping scenarios and add extra variability to collapse risk [3,16,17]. If a traditional single-dispersion representation is used without separating damper-related dispersion, the resulting estimates of annual collapse risk and acceptable CMR may be biased. This can misrepresent the true collapse safety margin of damped systems under extreme conditions.

Therefore, this study develops a risk-consistent method to determine the acceptable annual collapse probability and the corresponding acceptable CMR for viscous-damped structures under the CECS 392 hazard framework [18]. The method enables comparisons on a common scale across design intensities and structural importance categories. First, site-specific seismic hazard is coupled with collapse fragility. The annual collapse probability (or annual collapse rate) is used as the unified risk metric. This step establishes a quantitative mapping among the target risk, the total uncertainty, and the acceptable CMR. Next, the method explicitly addresses additional dispersion introduced by damper parameter variability, in-service degradation, and partial failures. Multi-stripe IDA results of the same structure are obtained under several representative damping scenarios. The variability of median collapse capacity across scenarios is identified and incorporated into the total collapse uncertainty. This treatment avoids the risk bias caused by using a single lumped dispersion. Finally, acceptable annual collapse-risk ranges and CMR target levels are provided for different design intensities, site conditions, and building importance categories. The framework can be used to quantify the actual contribution of supplemental damping to collapse safety margins. In its present form, it provides a code-linked and modular basis for design verification and post-assessment of viscous-damped structures. Its transferability arises from the replaceable hazard, fragility, and target-risk inputs embedded in the workflow, although broader validation beyond the present case study remains a subject for future work.

2. Decomposition and Incremental Identification of Collapse Uncertainty in Viscous-Damped Structures

2.1. Decomposition of Collapse Uncertainty and Nominal Total Dispersion σ_{base}

Collapse uncertainty is one of the key factors governing the acceptable CMR. For a given median collapse capacity and site-specific seismic hazard, a larger dispersion in the logarithmic intensity domain leads to a higher annual collapse rate from hazard–fragility convolution. To meet the same risk target, a larger collapse safety margin (CMR) is there-

fore required. In contrast, a smaller total uncertainty allows the target annual collapse probability to be achieved with a lower CMR.

Following ATC-63, this study decomposes structural collapse uncertainty into four components with explicit sources: record-to-record uncertainty σ_{RTR} (variability in response and collapse under different ground motions for the same structure), design- and requirement-related uncertainty σ_{DR} (ambiguity in collapse criteria and performance-threshold definitions), modeling uncertainty σ_{MDL} (bias and dispersion introduced by finite-element idealization, material and component constitutive models, connections, and numerical algorithms), and test-data uncertainty σ_{TD} (dispersion in material/component tests and extrapolation errors). Assuming these components are approximately independent with negligible correlation, the total uncertainty in the logarithmic intensity domain is obtained by variance summation and is denoted herein as σ_{base}.

$$\sigma_{base} = \sqrt{\sigma_{RTR}^2 + \sigma_{DR}^2 + \sigma_{MDL}^2 + \sigma_{TD}^2} \quad (1)$$

Here, σ_{base} denotes the nominal total uncertainty in collapse capacity when the additional variability associated with viscous dampers is not explicitly separated. Reported values of total collapse uncertainty in the literature commonly fall within 0.5–0.9. Accordingly, this study adopts $\sigma_{base} = 0.6$ as a representative value for the case-study structure, reflecting a typical level of collapse dispersion under conventional record selection, modeling assumptions, and test conditions. This point value is used as a representative anchor for the present case study, rather than as the sole uncertainty setting of the proposed framework. The practical sensitivity of acceptable CMR to total uncertainty is evaluated separately in Section 4.2 over the representative range $\sigma_{total,damp}$ = 0.50–0.90. For the present case study, this choice is further supported by the scenario analysis performed below. All damping scenarios are analyzed using the same ground-motion set, the same structural model, and the same collapse criterion; therefore, the major non-damper uncertainty sources embedded in σ_{base} remain unchanged across scenarios. In addition, the fitted within-scenario collapse dispersion is nearly identical for S0_NOM, S1_C × 0.8, and S2_FAIL7%, indicating that the dominant background variability of the present structure is stable. The observed differences in log-median collapse capacity among scenarios are small and are later shown to be comparable to their fitting standard errors, while the identified damper-induced incremental uncertainty remains limited within the degradation range considered in this study. Therefore, within the "mild degradation + limited partial failure" range considered in this study, the total collapse uncertainty remains essentially governed by the conventional baseline term, making σ_{base} = 0.60 a reasonable fixed reference for this case rather than a purely generic assumption. More severely deteriorated damping conditions may require re-evaluation in future applications. This choice also avoids introducing extra assumptions and uncertainty that would arise from separately regressing and estimating the four individual components.

2.2. Sources of Uncertainty in Viscous Dampers and Multi-Scenario IDA Design

In collapse assessment under strong earthquakes, conventional practice often follows ATC-63 and represents the combined effects of record selection, design requirements, modeling idealization, and test data by a single total uncertainty term to describe the overall dispersion of collapse capacity at a given intensity measure. This approach is mature for conventional structures without dampers. However, viscous-damped structures involve additional damper-related variability beyond these "general" sources. Typical contributors include manufacturing tolerances and in-service degradation of the damping coefficient, identification errors in the velocity exponent, force redistribution induced by installation quality and detailing, and localized failures such as sticking or leakage of

individual dampers. These factors may shift the representative level of collapse capacity and introduce extra dispersion across engineering scenarios. Simply lumping them into the conventional total dispersion, or neglecting them, undermines a quantitative assessment of the true contribution of damping systems to collapse safety margins. It also limits interpretable implications for damper design and maintenance.

To ensure that the identified incremental uncertainty σ_{damper} has clear engineering meaning, this study defines a set of representative damping scenarios. The case-study structure is a viscous-damped frame designed in accordance with CECS 392. Viscous fluid dampers are adopted, with nominal parameters of damping coefficient $C = 60\ \text{kN}/(\text{mm/s})^{\alpha}$ and velocity exponent $\alpha = 0.25$. The damper design also satisfies project constraints on peak damper force, displacement, and velocity.

Because practical applications more commonly involve mild degradation and a limited number of device issues, three scenarios are considered around the nominal configuration. Scenario S0_NOM is the nominal case, where all dampers operate with the design parameters. Scenario S1_C $\times$ 0.8 represents coefficient degradation, where C is uniformly reduced by 20% for all dampers, reflecting an overall efficiency loss that remains within an acceptable engineering range. Scenario S2_FAIL7% represents partial failure, where approximately 7% of dampers are randomly assumed to be out of service while the remaining dampers remain unchanged, characterizing a limited number of device issues rather than widespread failures.

These scenarios cover a typical path from nominal condition to mild global degradation and localized failures, while avoiding extreme deterioration conditions that are difficult to justify to stakeholders or codes. All scenarios use the same ground-motion set, modeling assumptions, and collapse criteria. In the IDA procedure, collapse is defined as the maximum interstory drift ratio exceeding 1/50. This drift-based threshold is adopted directly from CECS 392 as the engineering collapse criterion used in this study. Here, CECS 392 is used only to specify the collapse threshold itself for the IDA-based collapse judgment. In the present study, the record set is used as a common controlled excitation sample for comparative collapse assessment of the same structure under different damping scenarios, rather than as an independent definition of site hazard. Hazard consistency is maintained by adopting the same design/site setting, the same intensity measure $\text{Sa}(T_1)$, the same stripe configuration, and the same record set for all scenarios. Each record is amplitude-scaled to the target $\text{Sa}(T_1)$ level of each prescribed stripe in the multi-stripe IDA, so that collapse observations can be collected consistently across scenarios and intensity levels. The site hazard itself is introduced later in Section 3 through the code-consistent hazard representation constructed from the DBE and MCE control points. Multi-stripe IDA is then conducted to obtain collapse count data for subsequent identification of σ_{damper}.

To visually illustrate the response evolution under increasing ground-motion intensity across different damping scenarios, Figures 1–3 present the IDA curves for the three cases. Thin lines denote the IDA trajectories of individual records. Thick lines represent the 16th, 50th, and 84th percentile (P16, P50, and P84) envelopes, which describe record-to-record dispersion. The overall shapes are similar among the three scenarios. The curves nearly overlap at small drift levels. They gradually diverge as intensity increases. A clear "turning" behavior is observed near the collapse drift threshold. The P50 curve exhibits a monotonic S-shaped trend, indicating stable response evolution and good suitability for regression.

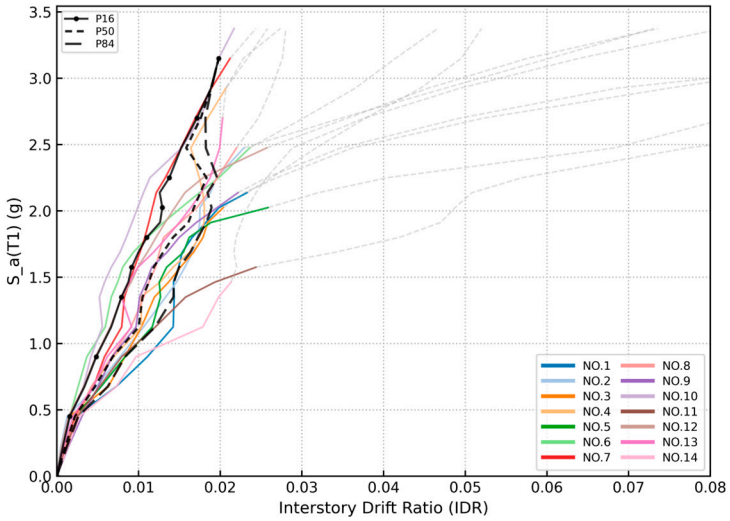


Figure 1. Incremental dynamic analysis (IDA) curves for the nominal damping scenario S0_NOM. The dashed grey lines indicate the divergent collapse stage beyond the corresponding points.

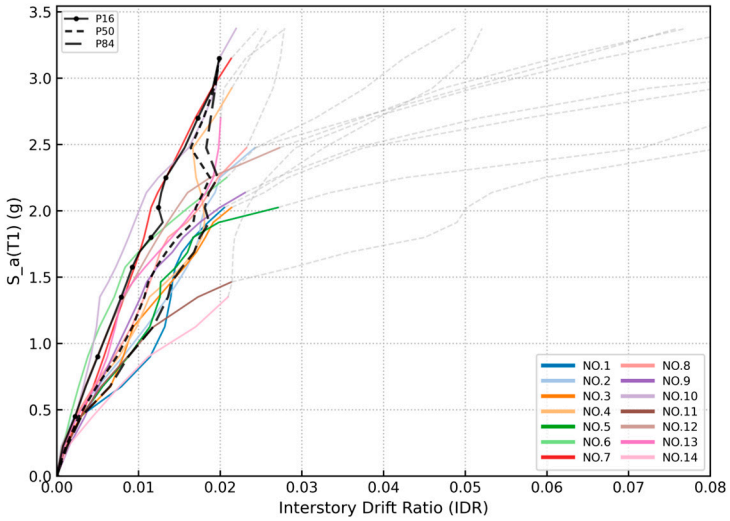


Figure 2. Incremental dynamic analysis (IDA) curves for the reduced-coefficient scenario S1_C × 0.8. The dashed grey lines indicate the divergent collapse stage beyond the corresponding points.

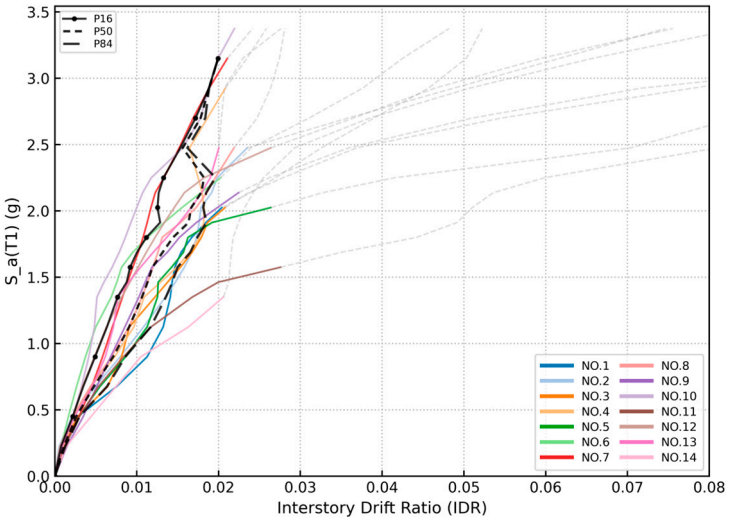


Figure 3. Incremental dynamic analysis (IDA) curves for the partial-failure scenario S2_FAIL7%. The dashed grey lines indicate the divergent collapse stage beyond the corresponding points.

Compared with the nominal case S0_NOM, the P50 curves of S1_C × 0.8 and S2_FAIL7% shift slightly to the left in the moderate-to-large drift range. This indicates larger interstory drift demands at the same $Sa(T_1, 5\%)$. The shift is consistent at the percentile-envelope level. It also agrees with the subsequent fragility results showing a 2–3% reduction in median collapse capacity for the weakened scenarios. It should be noted that the degradation settings adopted herein are intentionally mild yet representative. Accordingly, the observed differences mainly appear as a small downward shift in median capacity and a limited number of records collapsing earlier at high intensities. The magnitude of these differences is statistically identifiable while remaining realistic in engineering practice, providing a sound basis for the subsequent random-effects identification of the damper-induced incremental uncertainty.

2.3. Scenario-Based Collapse Fragility Modeling and Parameter Identification

To enable subsequent hazard convolution and the derivation of annual collapse rate, the discrete collapse counts from multi-scenario IDA must be represented by a continuous collapse fragility function, $P(\text{collapse}|\text{IM})$. Following ATC-63 and related studies, when the spectral acceleration at the fundamental period is used as the intensity measure, collapse fragility can be well described by a lognormal model. Therefore, a lognormal collapse fragility function is constructed for each damping scenario in this study.

Consider the same viscous-damped structure and define $m = 1, \cdots, M$ damping scenarios (e.g., S0_NOM, S1_C × 0.8, and S2_FAIL7%) under identical design, site, and record-selection settings. The same set of NNN ground motions is used to perform IDA for all scenarios. For scenario m, at intensity level $IM = x_i$, there are $n_{m,i}$ records and $y_{m,i}$ collapses, giving an empirical collapse probability $p_{m,i} = y_{m,i}/n_{m,i}$. Under the lognormal assumption, the collapse fragility for scenario m is expressed by Equation (2), where u_m is the true log-median collapse spectral acceleration for scenario m, $\phi(\cdot)$ is the standard normal CDF, and σ_{frag} is the within-scenario dispersion. The median collapse spectral acceleration is $S_{c,m} = \exp(u_m)$.

To identify these parameters from the observations $x_{i,j}$ and $p_{m,i}$, a generalized linear model (GLM) with a Probit link is adopted. The collapse probabilities $p_{m,i}$ are mapped to a linear predictor using the inverse link $\phi^{-1}(\cdot)$, yielding Equation (3), where a_m is the scenario-specific intercept and $b > 0$ is a common slope shared by all scenarios. A pooled fitting strategy is employed. All scenarios and all intensity-stripe observations $\left\{x_{i,j}, p_{m,i}\right\}$ are regressed simultaneously to ensure direct comparability across scenarios. In the present study, this common-slope formulation is adopted as a controlled comparative identification model under the same structure, the same record set, the same intensity measure $Sa(T_1)$, the same stripe configuration, and the same collapse criterion. For the intentionally mild scenario differences considered herein, this setting is used to isolate scenario-dependent shifts in μ_m while maintaining stable estimation precision for the subsequent random-effects identification of σ_{damper}.

$$P(collapse|IM = x, m) = \Phi\left(\frac{\ln x - \mu_m}{\sigma_{frag}}\right) \tag{2}$$

$$\Phi^{-1}(p_{m,i}) = a_m + b \ln x_i \tag{3}$$

Under the lognormal assumption, Equations (2) and (3) are equivalent. Equation (3) can be rearranged into Equation (4). Accordingly, the log-median collapse spectral acceleration for scenario m can be recovered from the scenario intercept $\hat{a}_m$ and the global slope $\hat{b}$ as $\hat{\mu}_m = -\hat{a}_m/\hat{b}$, with the estimated median collapse intensity $\hat{S}_{e,m} = \exp(\hat{\mu}_m)$. The within-scenario collapse dispersion is $\sigma_{frag} = 1/\hat{b}$.

The GLM fitting also provides the covariance matrix of the parameter vector $\left(\hat{a}_m, \hat{b}\right)$. Using the Delta method, the estimated variance of $\hat{\mu}_m = g\left(\hat{a}_m, \hat{b}\right) = -\hat{a}_m/\hat{b}$ can be obtained (Equation (5)), where ∇g is the gradient vector of g with respect to $\left(\hat{a}_m, \hat{b}\right)$. The standard error $S_{\mu,m}$ is then computed. It is used as the observation-precision input for the random-effects analysis in Section 2.4. Following this procedure, the identified fragility parameters for the three damping scenarios in the case study are summarized in Table 1.

$$\Phi^{-1}(p_{m,i}) = a_m + b \ln x_i = \frac{\ln x_i - \mu_m}{\sigma_{frag}} \tag{4}$$

$$s^2_{\mu,m} \approx \nabla g^{\top} \mathrm{Cov}\left(\hat{a}_m, \hat{b}\right) \nabla g \tag{5}$$

Table 1. Scenario-level collapse fragility parameters of the viscous-damped structure.

Scenario	Log-Median Collapse Spectral Acceleration $\hat{\mu}_m$	The Standard Error of $\hat{\mu}_m$,$S_{\mu,m}$	The Median Collapse Spectral Acceleration for Scenario m, $\hat{S}_{c,m}$	The Within-Scenario Collapse Dispersion σ_{frag}
S0_NOM	0.8077	0.0306	2.2428	0.2942
S1_C × 0.8	0.7810	0.0304	2.1837	0.2942
S2_FAIL7%	0.7869	0.0304	2.1966	0.2942

As shown in Table 1, the median collapse spectral acceleration of the nominal scenario S0_NOM is approximately 2.24 g. When the damping coefficient is reduced to 0.8C (S1_C × 0.8) or when 7% of the dampers are assumed to fail (S2_FAIL7%), the median collapse capacity decreases to about 2.18 g and 2.20 g, respectively, corresponding to a reduction of approximately 2–3%. The within-scenario collapse dispersion is nearly identical across the three scenarios, at about 0.29. For the present pooled comparative model, this means that the mild damping perturbations are expressed primarily through small scenario shifts in the identified median collapse capacity, rather than through pronounced slope separation of the fitted fragility curves. This indicates that, under a common ground-motion set and consistent modeling and collapse criteria, the within-scenario variability is still dominated by record-to-record fluctuations and incidental modeling effects. It should also be noted that the 14-record set used herein is intended for the present comparative and methodological application, rather than for a broad regional recalibration of collapse fragility. For this purpose, the dataset is considered adequate because the fitted log-median collapse capacities exhibit small standard errors (about 0.03 for all three scenarios), and the within-scenario dispersions remain highly consistent. These features indicate stable parameter identification under the common-record, common-IM, and common-stripe framework adopted in this study. Nevertheless, larger and more diverse record sets would be desirable in future studies aimed at broader fragility generalization or more refined hazard representation. It should also be noted that the identified median collapse capacity is conditional on the adopted collapse definition. In the present study, collapse is judged by the maximum interstory drift ratio exceeding 1/50. If a stricter collapse definition were adopted, the collapse points along the IDA curves would generally be reached at lower intensity levels, resulting in a lower estimated median collapse spectral acceleration. Conversely, a more relaxed collapse definition would tend to increase the estimated median collapse capacity. Therefore, the absolute value of the median collapse capacity is criterion-dependent, although the relative comparison among the three damping scenarios remains internally consistent because the same collapse criterion is applied throughout the study. In contrast,

mild degradation of damper parameters primarily manifests as a small downward shift in median collapse capacity rather than a significant increase in dispersion.

The corresponding collapse fragility curves are shown in Figure 4. All three curves are well represented by monotonic S-shaped functions. Under the common-dispersion assumption, the weakened scenarios exhibit a slight leftward shift relative to S0_NOM, while the curve slopes remain approximately the same. This representation is adopted here for controlled scenario comparison in the present mild-perturbation setting; for broader degradation spaces or richer failure patterns, models with scenario-specific slopes β_m may be examined in future studies.

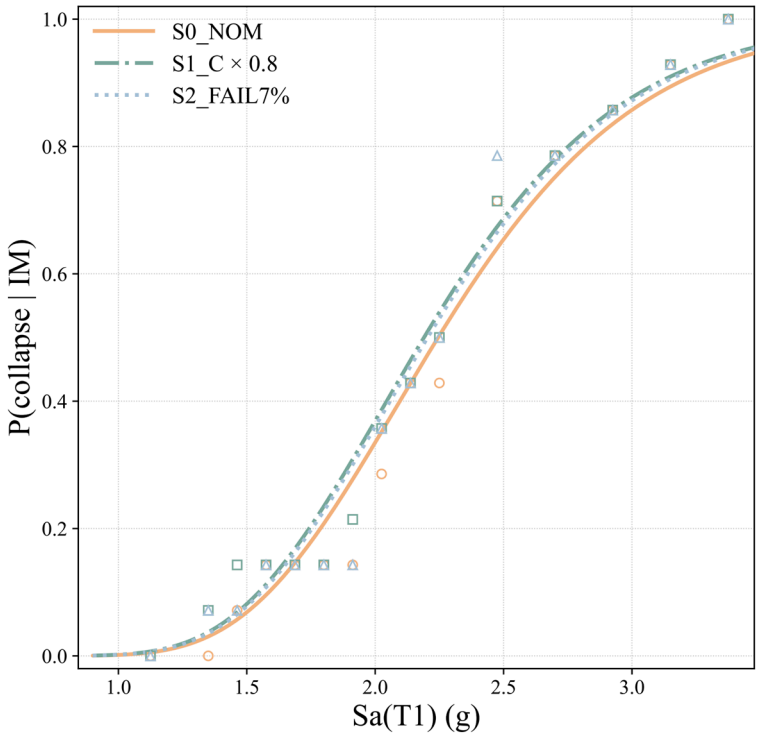


Figure 4. Collapse fragility curves of the viscous-damped structure under three damping scenarios. Hollow markers denote the collapse probabilities at the corresponding $\mathrm{Sa}(\mathrm{T}_1)$ levels.

In summary, the values of $\hat{\mu}_m$, $s_{\mu,m}$, and σ_{frag} reported in Table 1 provide stable inputs for the subsequent random-effects decomposition. They quantify both the representative level of collapse capacity and its estimation precision for different damping scenarios. These results allow the scenario-specific medians to be treated as samples with measurement error, forming the basis for identifying the damper-induced incremental uncertainty σ_{damper} and for combining it with the baseline uncertainty σ_{base} to obtain the total collapse uncertainty $\sigma_{total,damp}$.

2.4. Damper-Induced Incremental Uncertainty and Total Collapse Uncertainty

Consider the log-median collapse capacity of each damping scenario in the logarithmic intensity domain, $\mu_m = \ln S_{c,m}$ All damping scenarios are treated as realizations fluctuating around a common population level. Accordingly, the log-median collapse spectral acceleration $\hat{\mu}_m$ can be expressed in the decomposed form given by Equation (6):

$$\hat{\mu}_m = \mu + \delta_m + \varepsilon_m \tag{6}$$

Here, μ denotes the overall mean of the log-median collapse spectral acceleration across all damping scenarios; σ_m represents the systematic deviation of the m-th damping

scenario from the overall mean; and ε_m is the statistical error induced by the finite number of records and the GLM fitting procedure.

In this study, $\delta_{\mathrm{m}} \sim \mathrm{N}\left(0, \sigma^2_{\mathrm{damper}}\right)$ and $\varepsilon_{\mathrm{m}} \sim \mathrm{N}\left(0, \sigma^2_{\mu,\mathrm{m}}\right)$ are assumed. That is, the systematic differences among damping scenarios are modeled as zero-mean normal random effects, while $\mathrm{S}_{\mu,\mathrm{m}}$ is taken as the standard error of $\hat{\mu}_{\mathrm{m}}$ obtained from the Probit regression in Section 2.3. Accordingly, the subsequent identification of σ_{damper} is based on the dispersion of the scenario-level log-median capacities μ_{m} after accounting for their estimation errors, rather than on an independent scenario-by-scenario comparison of fitted fragility slopes. Under these assumptions, $\hat{\mu}_{\mathrm{m}}$ can be expressed as Equation (7):

$$\hat{\mu}_m \sim N\left(\mu, s^2_{\mu,m} + \sigma^2_{damper}\right) \tag{7}$$

Here, σ_{damper} denotes the incremental uncertainty induced by viscous dampers. After removing estimation error, it quantifies the dispersion of the log-median collapse capacity among damping scenarios, including the nominal case, damping-coefficient degradation, and partial failure. If variations in damper parameters have a pronounced effect on collapse capacity, σ_{damper} will be large; otherwise, it will approach zero.

To robustly identify σ_{damper} from a limited number of scenario observations $\left\{\hat{\mathrm{u}}_{\mathrm{m}}, \mathrm{S}_{\mu,\mathrm{m}}\right\}$, a two-step strategy of "DL initialization + REML refinement" is adopted. First, the scenario-specific variances $\mathrm{s}^2_{\mu,\mathrm{m}}$ are treated as known observation errors. Inverse-variance weights $\mathrm{w}_{\mathrm{m}} = 1/\mathrm{s}^2_{\mathrm{u,m}}$ are constructed, and the weighted overall mean is estimated (Equation (8)). The Cochran heterogeneity statistic is then defined (Equation (9)), together with the correction term (Equation (10)). The DerSimonian–Laird random-effects model yields an initial estimate of the between-scenario variance as given by Equation (11).

$$\hat{\mu}_{\mathrm{eq}} = \frac{\sum_{m=1}^{M} w_m \hat{\mu}_m}{\sum_{m=1}^{M} w_m} \tag{8}$$

$$Q = \sum_{m=1}^{M} w_m (\hat{\mu}_m - \hat{\mu}_{eq})^2 \tag{9}$$

$$C = \sum_{m=1}^{M} w_m - \frac{\left(\sum_{m=1}^{M} w_m\right)^2}{\sum_{m=1}^{M} w_m^2} \tag{10}$$

$$\tau^2_{DL} = \max\left\{0, \frac{Q - (M-1)}{C}\right\} \tag{11}$$

When Q is not significantly greater than $\mathrm{M} - 1$, Equation (11) automatically truncates τ^2_{DL} to zero. This corresponds to the case where between-scenario differences are statistically negligible. Because the number of scenarios M in this study is small, the DerSimonian–Laird estimator may be sensitive to sample size. Therefore, a restricted maximum likelihood (REML) approach is further adopted within a normal mixed-effects framework to refine the estimate of $\sigma^2_{\mathrm{damper}}$. Using τ^2_{DL} as the initial value, the REML log-likelihood function $\ell_{\mathrm{REML}}\left(\hat{\sigma}^2_{\mathrm{damper}}\right)$ is constructed. The first-order optimality condition is then solved numerically to obtain τ^2_{REML} (Equation (12)). The final damper-induced incremental uncertainty σ_{damper} is given by Equation (13).

$$\frac{\partial \ell_{REML}}{\partial \sigma^2_{damer}} = 0 \tag{12}$$

$$\sigma_{damper} = \sqrt{\tau^2_{REML}} \tag{13}$$

After identifying σ_{damper}, it is combined with the baseline collapse uncertainty of the structure, σ_{base}. The latter represents the aggregated effect of multiple uncertainty sources—such as record selection, modeling assumptions, numerical procedures, and collapse criteria—when damper degradation and failure are not explicitly distinguished. Following ATC-63 and related recommendations, σ_{base} is constrained to a reasonable range of [0.5, 0.9]; in this case study, $\sigma_{\text{base}} = 0.60$ is adopted. Because σ_{base} and σ_{damper} originate from nominal structural uncertainty and damping-scenario differences, respectively, they can be treated as approximately independent components. Accordingly, the total collapse uncertainty in the logarithmic intensity domain is obtained by variance summation, as given in Equation (14).

$$\sigma_{total,damp} = \sqrt{\sigma_{base}^2 + \sigma_{damper}^2} \tag{14}$$

Based on the fragility parameters of the three damping scenarios reported in Table 1, the additional uncertainty introduced by the dampers is decomposed and quantified, with the results summarized in Table 2. For the case study, $\sigma_{\text{base}} = 0.60$ is adopted. Thus, the case-study value $\sigma_{\text{base}} = 0.60$ serves as a representative anchor for the analyzed structure, rather than the sole uncertainty setting of the proposed framework. The random-effects decomposition yields $\sigma_{\text{damper}} \approx 0$, and consequently $\sigma_{\text{total,damp}}$ remains close to 0.60. This indicates that, under the considered mild degradation level (20% reduction in damping coefficient combined with 7% partial failures), the damping conditions contribute only marginally to the overall dispersion. This result also provides case-specific retrospective support for the fixed use of $\sigma_{\text{base}} = 0.60$: once the scenario-induced incremental uncertainty is found to be limited for the considered scenario set, the total collapse uncertainty of the present structure is still governed primarily by the baseline term associated with conventional non-damper sources.

Table 2. Decomposition of damping-related and total collapse uncertainty.

σ_{base}	σ_{damper}	$\sigma_{\text{total,damper}}$	τ^2_{DL}	τ^2_{REML}
0.6	0	0.6	0	0

This finding is consistent with the characteristics observed in Table 1. The differences in μ_{m} among the three scenarios are on the order of 0.02–0.03, while their standard errors are approximately 0.03. Thus, the between-scenario shifts in median collapse capacity are comparable to the fitting uncertainty, and the within-scenario record-to-record variability remains the dominant source of dispersion.

Therefore, in the subsequent derivation of the annual collapse rate and the acceptable CMR, $\sigma_{\text{total,damp}} \approx \sigma_{\text{base}}$ is adopted as the representative dispersion parameter. The primary role of viscous dampers is thus interpreted as increasing the median collapse capacity (Table 1), rather than substantially amplifying the total uncertainty. This result also provides quantitative support for a common engineering understanding: when viscous dampers are properly designed and maintained, parameter degradation and limited device failures have a relatively minor effect on overall collapse uncertainty, while their more significant contribution lies in enhancing the collapse-prevention safety margin of the structure.

3. Derivation of the Annual Collapse Rate and Acceptable CMR for Viscous-Damped Structures

Earthquake ground motions are inherently stochastic. Evaluating collapse performance only at a specified hazard level (e.g., DBE or MCE) using collapse probability is essentially a conditional point estimate. Such an approach neither accounts for the annual occurrence rates of earthquakes with different intensities and their cumulative contribu-

tions to annual collapse risk, nor prevents random fluctuations associated with extremely rare events from being overstated.

To ensure consistency between collapse-performance evaluation and the design service life, this study introduces the site-specific seismic hazard $\lambda(\mathrm{IM} \geq \mathrm{x})$, defined as the annual exceedance rate of the intensity measure IM beyond a threshold. This hazard function serves as a frequency weighting in the intensity domain and is convolved with the structural collapse fragility to obtain the annual collapse rate λ_c (or equivalently, the annual collapse probability). Collapse-prevention design and acceptability checks are then performed using a unified annual risk target.

3.1. Annual Collapse Probability

Under the Poisson assumption, the exceedance probability p_t over a time window t and the corresponding annual rate λ satisfy:

$$\lambda = -\frac{\ln(1 - p_t)}{t} \tag{15}$$

For t = 50 years, p_{50} = 10% and 2% correspond to λ = 0.002105/year and 0.000404/year, respectively.

3.2. Power-Law Fitting of Site Seismic Hazard

The site seismic hazard curve provides the annual exceedance rate of the intensity measure IM beyond any threshold x. To facilitate analytical derivations, a local power-law approximation is adopted over the collapse-relevant intensity range:

$$\lambda(IM \geq x) = k_0\, x^{-k} \tag{16}$$

Let the 50-year exceedance probabilities associated with DBE and MCE be $p_D = 10\%$ and $p_M = 2\%$, respectively. Using Equation (15), the corresponding annual exceedance rates are λ_D and λ_M.

The intensity measure is taken as $\mathrm{IM} = S_a(T_1, 5\%)$. The code-specified DBE and MCE spectral intensities at T_1 are denoted by $x_D = S_a(10\%, 50a; T_1)$ and $x_M = S_a(2\%, 50a, T_1)$, respectively. With these two points, the parameters of the power-law hazard model can be determined:

$$k = \frac{\ln(\lambda_M/\lambda_D)}{\ln(x_D/x_M)}, k_0 = \lambda_D\, x_D^k \tag{17}$$

Here, k and k_0 represent the shape and scale of the hazard curve, respectively. The parameter k can be interpreted as the decay slope in the logarithmic domain, while k_0 is the scale factor, i.e., the annual exceedance rate when (x = 1).

Based on the CECS 392 design spectrum and using $S_a(T_1, 5\%)$ as the intensity measure, hazard curves were derived for design intensities of 6–9, with T_1 = 0.3 s, Site Class II, and T_g = 0.4 s (Figure 5). As the design intensity increases, the plateau spectral ordinates increase, leading to a systematic rightward shift of the hazard curve. This implies a higher annual exceedance rate at a given intensity threshold. Conversely, for a fixed target annual rate, a larger intensity level is required. Meanwhile, as the ratio x_M/x_D decreases, the slope parameter k increases, and the curves exhibit a steeper decay in semi-log coordinates. In other words, in higher-intensity regions the annual occurrence rate of very large ground motions decays more rapidly with intensity. However, due to the overall rightward shift, the annual exceedance level at the same threshold can still be higher than that in lower-intensity regions.

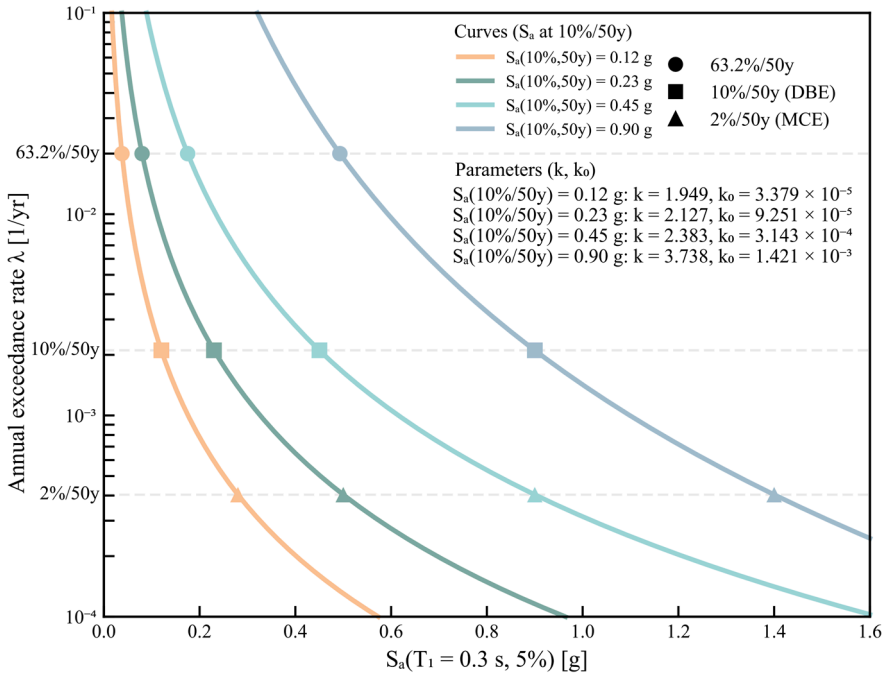


Figure 5. Site seismic hazard curves under different design intensities.

It should be noted that the power-law hazard model adopted herein is a two-point, code-consistent engineering representation anchored at the DBE and MCE control points, rather than a regression to a dense continuous hazard dataset. Therefore, the approximation is exact at the two anchor points by construction, and the main issue is not residual fitting error at those points but possible model-form deviation between and beyond them. In the present study, the annual collapse-rate evaluation is governed mainly by the intensity range relevant to collapse, i.e., from the upper design level to the neighborhood of the identified median collapse intensities of the three damping scenarios. Within this range, the power-law form provides a transparent local approximation that enables the closed-form hazard–fragility convolution in Equation (20) and the inversion to acceptable CMR in Equation (24). If the actual hazard curve decays more slowly than the adopted power law in the collapse-relevant tail, the annual collapse rate will be underestimated and the resulting acceptable CMR will also be underestimated; conversely, a faster actual decay would lead to conservative CMR estimates. Accordingly, the results of the present study should be interpreted as conditional on the adopted local two-point hazard representation. When denser site-specific hazard data are available, the same framework can be refined by recalibrating the local hazard parameters or by using a more detailed hazard representation.

In addition, as shown in Figure 6, the differences among hazard curves for different T_1 values are mainly reflected in the scale parameter λ_0. As T_1 increases, the hazard curve shifts to the right, and the annual exceedance rate λ at a given $\mathrm{Sa}(\mathrm{T}_1)$ decreases markedly. Relative to $\mathrm{T}_1 = 0.3$ s, the scale parameters for $T_1 = 1.5$ s and 3.0 s drop to approximately 1/17 and 1/39 of that value, respectively, indicating a pronounced risk-reduction effect associated with period lengthening.

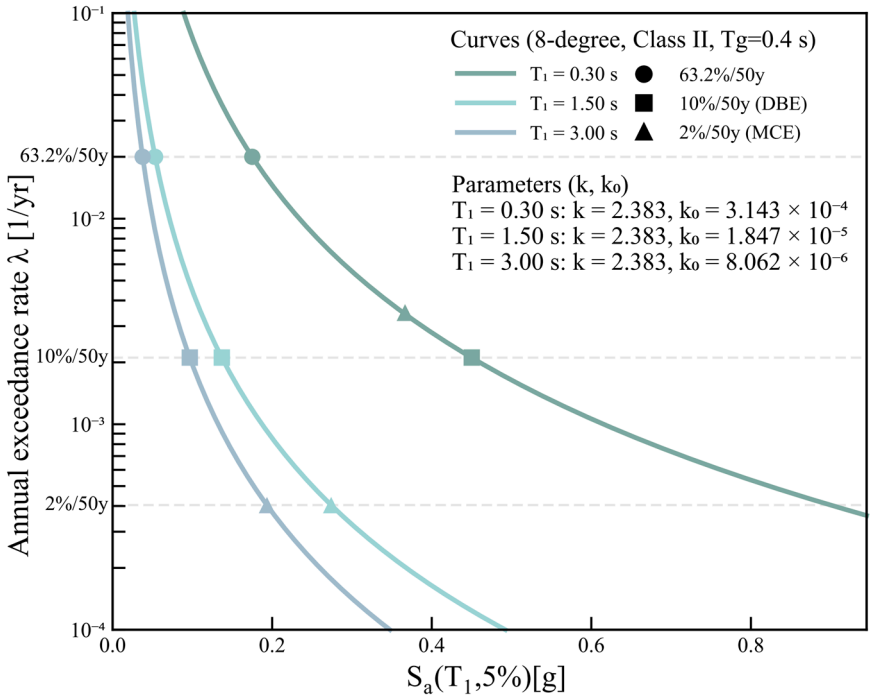


Figure 6. Site seismic hazard curves for different fundamental periods (T1).

In other words, the period effect is mainly manifested as a horizontal shift in the hazard level rather than a change in curve shape. When damping, isolation, or yielding increases the effective period of a structure, a lower annual exceedance rate can be obtained from the hazard perspective alone, even without accounting for changes in fragility.

3.3. Closed-Form Expression for Hazard–Fragility Convolution

Following the fragility expression in Equation (2), after identifying the total collapse uncertainty $\sigma_{\text{total,damp}}$ across scenarios, the scenario subscript m is omitted. An equivalent collapse fragility function is then constructed using the overall log-median capacity μ and the total dispersion $\sigma_{\text{total,damp}}$:

$$P(collapse \mid IM = x) = \Phi\left(\frac{\ln x - \mu}{\sigma_{total,damp}}\right) \tag{18}$$

Here, $\hat{S}_c$ is the median collapse spectral acceleration corresponding to 50% collapse probability, and $\sigma_{\text{total,damp}}$ is the total collapse uncertainty of the viscous-damped structure.

Under the Poisson assumption, the annual collapse rate can be obtained from the total-probability integral over the intensity domain:

$$\lambda_c = \int_0^{\infty} P(collapse \mid x)\, \mathrm{d}\lambda(x) \tag{19}$$

Substituting the power-law hazard model in Equation (16) and applying a variable transformation in the logarithmic domain, the convolution can be reduced to the expectation of an exponential function of a normal random variable. This leads to the following closed-form solution:

$$\lambda_c = k_0\, \hat{S}_c^{-k} \exp\left(\frac{1}{2} k^2 \sigma^2_{\text{total,damp}}\right) \tag{20}$$

Equation (20) directly yields two first-order sensitivities, which are used to discuss the effects of uncertainty and median capacity:

$$\frac{\partial \ln \lambda_c}{\partial \mu} = -k, \frac{\partial \ln \lambda_c}{\partial \sigma} = k^2 \sigma_{total,damp} \tag{21}$$

3.4. Minimum Median Capacity and Acceptable CMR

In viscous-damped design, the requirement is $\lambda_c\left(\hat{S}_c, \sigma_{total,damp}\right) \leq \hat{\lambda}_c$. At the critical condition $\lambda_c = \hat{\lambda}_c$, back-substituting from Equation (20) and exponentiating gives the minimum median collapse capacity required to meet the target risk:

$$\hat{S}_{c,min}\left(\sigma_{total,damp}\right) = \left(\frac{k_0}{\lambda_c}\right)^{1/k} \exp\left(\frac{1}{2} k \sigma^2_{total,damp}\right) \tag{22}$$

Here, $\hat{S}_{c,min}$ is the minimum median collapse intensity (at 50% collapse probability) required to satisfy the target annual risk.

To facilitate consistency with the design spectrum, $\hat{S}_{c,min}$ is normalized by the code spectral intensity $S_{a,g}(T_1)$ for a given level (g) (DBE or MCE), yielding the acceptable CMR relative to DBE/MCE:

$$CMR^{(g)}_{min}\left(\sigma_{total,damp}\right) = \frac{\hat{S}_{c,min}\left(\sigma_{total,damp}\right)}{S_{a,g}(T_1)} \tag{23}$$

Here, $S_{a,g}(T_1)$ is the spectral acceleration at period T_1 for level (g).

Substituting Equation (22) into Equation (23) and using the equivalent relationship from the power-law hazard model (Equation (16)), $k_0 = \lambda\left\{IM \geq S^k_{a,g}\right\} S^k_{a,g}$, the expression can be rewritten into a practical form that does not explicitly involve k_0:

$$CMR^{(g)}_{min} = \left(\frac{\lambda\left(IM \geq S_{a,g}\right)}{\hat{\lambda}_c}\right)^{1/k} \exp\left(\frac{1}{2} k \sigma^2_{total,damp}\right) \tag{24}$$

4. Socially Acceptable Collapse Probability and Acceptable CMR

4.1. Socially Acceptable Collapse Probability

Based on the site-specific seismic hazard curve fitted in Section 3.2 (Equation (16)) and the hazard–fragility convolution framework established in Equations (18)–(21), this section converts the conditional collapse-probability limits specified in current codes (point-based constraints) into socially acceptable annual collapse rates $\hat{\lambda}_c$ (or equivalently, annual collapse probabilities). This enables a direct comparison between the annual collapse rate $\lambda_c\left(\hat{S}_c, \sigma_{total,damp}\right)$ computed for any viscous-damped structure and the target $\hat{\lambda}_c$. The acceptable CMR level required to satisfy the societal risk objective can then be obtained by inverting Equations (22)–(24).

For clarity, the seismic design intensity is represented by the basic ground acceleration PGA (g) of the design-basis earthquake (DBE): 6°, 7°, 7.5°, 8°, 8.5°, and 9° correspond to 0.05 g, 0.10 g, 0.15 g, 0.20 g, 0.30 g, and 0.40 g, respectively. In addition, "Category B buildings" refer to important buildings for which post-earthquake functionality should be restored rapidly or should not be interrupted, whereas "Category C buildings" refer to standard buildings (general public buildings) designed according to conventional seismic provisions.

4.1.1. FEMA/ATC-63 Framework

Within the FEMA/ATC risk-consistent collapse framework, acceptable collapse risk is commonly constrained at two levels. The first is a life-cycle risk target, such as the "no more than 1% probability of collapse in 50 years" requirement for ordinary buildings adopted in FEMA P-750 and ASCE 7-10 [19,20]. Under the Poisson-process approximation for collapse occurrence, this requirement can be converted into an equivalent upper bound on the annual collapse rate.

The second is a conditional collapse-probability limit at a strong-motion level. ATC-63 further recommends that the conditional collapse probability at the MCE level be controlled on the order of 10%. In the proposed framework, this can be treated as a point constraint on Equation (18). Specifically, let IM be the spectral acceleration corresponding to MCE. For a given total collapse uncertainty $\sigma_{\text{total,damp}}$, enforce $P(\text{collapse} \mid \text{IM} = \chi) = \Phi\left(\frac{\ln x - \mu}{\sigma_{\text{total,damp}}}\right) = P_{\text{MCE}} \approx 10\%$. This relation can be inverted to obtain the median capacity $\hat{S}_{c,\text{ATC}}$ required to satisfy the limit. Substituting $\hat{S}_{c,\text{ATC}}$ into Equation (20) yields the annual-collapse-rate target $\lambda_{c,\text{ATC}} = \lambda_c\left(\hat{S}_{c,\text{ATC}}, \sigma_{\text{total,damp}}\right)$, which is risk-equivalent to the ATC-63 conditional limit and can be used for consistency checks against ATC-63 recommendations.

4.1.2. CECS 392 Framework (China)

In the Chinese Technical Specification for Collapse-Resistant Design of Building Structures (CECS 392), the code directly specifies the maximum acceptable conditional collapse probabilities under the "rare earthquake" and the "very rare earthquake" levels (Table 3). In this study, these limits are converted to the annual scale for both Category C (standard) buildings and Category B (important) buildings.

Table 3. Maximum acceptable conditional collapse probability in CECS 392 (%).

Earthquake Level	Category C Buildings	Category B Buildings
Rare earthquake	5	1
Very rare earthquake	10	5

For clarity, the "Rare earthquake" level in CECS 392 is referred to hereafter as the MCE level, while the "Very rare earthquake" level retains the same designation in the subsequent tables and charts. For a given seismic design intensity (6–9°), site class, and characteristic period (Site Class III, the third seismic group, and $T_g = 0.65$ s in this study), Equation (18) is evaluated at $x = S_a^{(g)}(T_1, 5\%)$. By imposing $P(\text{collapse}|\text{IM} = x) = P_{C,\text{CECS}}^{(g,\text{class})}$, the minimum median collapse capacity required to satisfy CECS 392 can be back-calculated (Equation (25)). Using the power-law hazard parameters k_0 and k fitted in Section 3.1 for the corresponding design intensity and structural period, $\hat{S}_{c,\min}^{(g,\text{class})}(T_1)$ is then substituted into Equation (20). This yields the socially acceptable annual collapse rate for that combination (Equation (26)).

$$\hat{S}_{c,\min}^{(g,class)}(T_1) = S_a^{(g)}(T_1, 5\%) \exp\left[-t_x^{(g,class)} \sigma_{total,damp}\right] \tag{25}$$

$$\hat{\lambda}_c^{(g,class)}(T_1) = \lambda_c\left(\hat{S}_{c,\min}^{(g,class)}(T_1), \sigma_{total,damp}\right) \tag{26}$$

Here, $t_x^{(g,\text{class})} = \Phi^{-1}\left(P_c^{(g,\text{class})}\right)$ is the standard normal quantile corresponding to the code-specified conditional collapse probability.

Following the above procedure, point-by-point calculations are performed for all combinations of design intensity 6–9° (PGA = 0.05–0.40 g), building category (C/B), and

earthquake level (rare/very rare). This yields the CECS 392-based socially acceptable annual collapse rates, as summarized in Table 4.

Table 4. CECS-based socially acceptable annual collapse rate $\hat{\lambda}_c(\times 10^{-4}\mathrm{yr}^{-1})$.

Seismic Category	Earthquake Level	0.05 g	0.10 g	0.15 g	0.20 g	0.30 g	0.40 g
Category C	Rare (MCE)	1.169	1.118	1.101	1.069	1.050	1.016
	Very rare	1.096	0.818	0.863	0.684	0.448	0.359
Category B	Rare (MCE)	0.527	0.469	0.448	0.404	0.320	0.271
	Very rare	0.487	0.434	0.415	0.357	0.238	0.159

As shown in Table 4, for the same design intensity, the acceptable annual collapse rate $\hat{\lambda}_c^{(\mathrm{MCE})}$ for Category C buildings is about twice that for Category B buildings. This is because CECS 392 specifies a stricter conditional collapse-probability limit for Category B buildings (e.g., $(P_{C,MCE} = 1\%)$) than for Category C buildings (e.g., $(P_{C,MCE} = 5\%)$). The resulting difference reflects the intended risk control hierarchy in the code. It is also consistent with the functional classification in CECS 392, where Category B corresponds to lifeline/important-function buildings and Category C corresponds to general public buildings.

Along the design-intensity axis, the acceptable annual collapse rate shows a mild overall decrease as intensity increases from 6° to 9° for the same building category. For Category C under MCE, $\hat{\boldsymbol{\lambda}}_{\mathbf{c}}$ decreases from 1.17×10^{-4} to 1.02×10^{-4}. For Category B under MCE, it decreases from 0.53×10^{-4} to 0.27×10^{-4}. This "slightly tighter control at higher intensity" arises from the power-law decay of the hazard model $\lambda(S_a)$. In higher-intensity regions, satisfying the same pointwise conditional-collapse limit requires larger spectral intensities $S_{a,MCE}$ and $S_{\alpha,V_{rare}}$. When mapped through the hazard–fragility convolution, this leads to a slightly lower annual collapse-rate target, indicating more conservative risk control at higher design intensities. Small adjustments at a few points (e.g., Category C under MCE at 8.5° versus 9°) are within about 5% and mainly result from combined fitting differences in k and k_0. These minor non-monotonic variations are not practically significant and can be regarded as the same order of risk requirement.

For a fixed design intensity and building category, the acceptable annual collapse rate associated with the very rare earthquake level is consistently lower than that associated with the rare earthquake level. For example, at 8°, Category C decreases from 1.07×10^{-4} to 0.68×10^{-4}, and Category B decreases from 0.40×10^{-4} to 0.36×10^{-4}. This reflects the risk-tiering philosophy of CECS 392: under more extreme and rarer hazard levels, the code requires a lower annual collapse-rate target to compensate for the amplified consequences and uncertainty associated with extreme ground motions. Compared with the uniform control value of 2.0×10^{-4} in FEMA P-750, the CECS-based acceptable annual collapse rates for both Category B and Category C buildings are generally lower for most intensity combinations. This suggests that, within the Chinese seismic-design context, CECS 392 implies an overall more conservative level of collapse-risk control.

4.2. Acceptable CMR

Based on the socially acceptable annual collapse rates $\hat{\lambda}_c^{(g,\mathrm{class})}$ in Table 4, Equation (24) is used to compute the acceptable minimum collapse margin ratio, CMR_{min}, for different design intensities, building categories, and hazard levels (Rare (MCE)/Very rare). A representative range of $\sigma_{total,damp} = 0.50 \sim 0.90$ is considered to show directly how the required acceptable CMR propagates with uncertainty level around the case-study anchor. The resulting CMR_{min} values for Category C and Category B buildings are shown in

Figure 7. These values represent the minimum collapse safety margins required to keep the annual collapse risk within socially acceptable limits under the CECS 392 collapse-probability constraints.

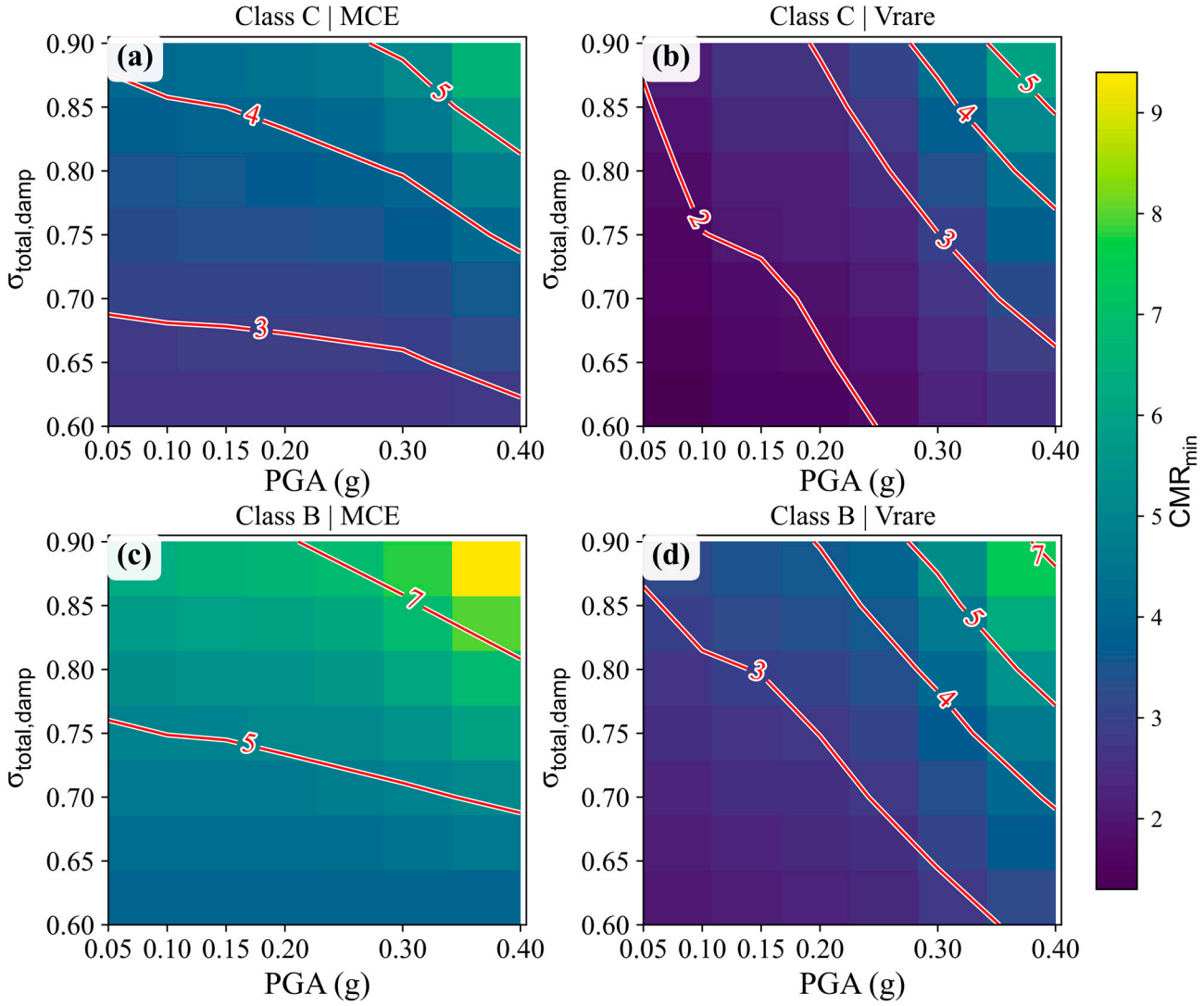


Figure 7. Design charts of the acceptable minimum collapse margin ratio, CMR_{min}, as a function of peak ground acceleration (PGA) and total collapse uncertainty $\sigma_{total,damp}$ for (**a**) Class C under MCE, (**b**) Class C under Vrare, (**c**) Class B under MCE, and (**d**) Class B under Vrare. A unified color scale is used across panels to enable direct comparison. Red contour lines denote iso-CMRmin values, and the red numbers indicate the corresponding contour levels.

From the perspective of building category, for the same design intensity, the same $\sigma_{total,damp}$, and the same hazard level, Category B buildings generally require markedly higher acceptable CMR than Category C buildings. For example, under MCE, when $\sigma_{total,damp}$ is at a moderate level (around 0.75), CMR_{min} is approximately 3 for Category C buildings, whereas Category B buildings often require CMR values around 5 or higher to satisfy the smaller acceptable annual collapse rates prescribed by the code. This difference is a direct consequence of the stricter collapse-probability limits for Category B buildings in CECS 392. In Equation (24), a smaller target annual collapse rate leads to a stronger amplification in CMR_{min}. Therefore, Category B buildings face higher collapse-safety requirements under the same damping measures and must provide larger collapse margins to achieve a "socially acceptable" risk level.

From the perspective of total collapse uncertainty, CMR_{min} shows a pronounced nonlinear amplification with increasing $\sigma_{total,damp}$. For a fixed design intensity and building category, increasing $\sigma_{total,damp}$ from 0.50 to 0.90 typically raises CMR_{min} by about 1.5–2 times. This amplification becomes more evident at higher design intensities and under stricter hazard-level requirements. The trend is consistent with the exponential term $\exp\left(\frac{1}{2}k\sigma^2_{total,damp}\right)$ in Equation (24). As uncertainty increases, the annual collapse rate becomes more sensitive to perturbations in median capacity. To maintain the same acceptable annual collapse probability, CMR_{min} must increase to offset the "erosion" of safety margins caused by uncertainty. This effect is most pronounced for the most stringent combinations, such as Category B under the very rare earthquake level, indicating that meeting code targets under high uncertainty can entail substantially higher design margins.

Considering design intensity and hazard level, CMR_{min} exhibits different patterns under MCE and the very rare earthquake level. For Category C buildings, CMR_{min} under MCE varies moderately from 6° to 8° and increases only slightly toward 9°. This suggests that, near the selected period range, the changes in hazard level and acceptable collapse-probability limits in CECS 392 are broadly balanced, leading to limited variation in the ratio $\lambda(IM \geq S_{a,g})/\hat{\lambda}_c^{(g)}$ in Equation (24). In contrast, under the very rare level, the acceptable annual collapse rate tightens more noticeably with increasing design intensity, driving a monotonic increase in CMR_{min}. At high design intensities, CMR_{min} approaches or exceeds the ATC-63 lower bound of 2.0. For Category B buildings, the same tendencies are more pronounced due to stricter limits: CMR_{min} is higher under MCE overall, and under the very rare level it can reach approximately 5–7 at high design intensities, reflecting the elevated collapse-margin demand for important buildings.

In summary, by combining the CECS 392 collapse-probability limits with the analytical annual collapse rate–CMR relationship developed in Section 3.2, this study establishes an acceptable-CMR calibration framework that explicitly depends on design intensity, building category, and total collapse uncertainty $\sigma_{total,damp}$ Compared with applying a single CMR lower bound from ATC-63, the proposed framework distinguishes the risk tolerance across Category C/Category B buildings and across MCE/very rare hazard levels, and it quantitatively reveals the amplification effect of uncertainty on the required collapse margin. The resulting design charts provide a practical tool for damping applications: for a given target annual collapse rate, the required CMR can be back-calculated and used to verify damper configuration and design margins, enabling risk-consistent control of collapse-prevention safety reserves.

For iterative design use, the charts are intended as a rapid check under the current design state rather than a fixed once-for-all lookup. Starting from a trial scheme, the engineer updates the period-dependent hazard parameters and the total collapse uncertainty for the current structural and damping configuration, reads the required acceptable CMR from Figure 7 (or equivalently from Equation (24)), and compares it with the actual CMR of the scheme. When revisions to structural stiffness, member sizes, structural layout, or damping properties alter these governing inputs, the chart should be revisited accordingly. The above chart-based results are established for the present study setting, namely a code-designed viscous-damped RC frame with three engineering-representative scenarios in a mild degradation and limited partial-failure range, a common 14-record set for fragility identification, a two-point power-law hazard representation anchored at the DBE and MCE levels, and the adopted drift-based collapse criterion. Therefore, these charts should be interpreted as rapid-check tools conditional on the adopted local hazard representation.

5. Conclusions

(1) Building on the conventional collapse-uncertainty framework, this study groups record-to-record, modeling, and material effects into a baseline collapse uncertainty σ_{base}, and separately abstracts the additional dispersion induced by damping-coefficient degradation and partial failures as a damper-induced incremental uncertainty σ_{damper}. Their orthogonal combination yields the total collapse uncertainty of viscous-damped structures,$\sigma_{total,damp}$, clearly delineating the roles of background dispersion and damping-scenario differences in collapse-risk assessment.

(2) For three engineering-representative damping scenarios—nominal damping, coefficient degradation, and partial failure—multi-stripe IDA is conducted using a common ground-motion set and collapse criteria. Scenario-wise lognormal fragilities are fitted to obtain median capacities and standard errors. A random-effects model with "Der Simonian–Laird initialization + REML refinement" is then used to estimate between-scenario dispersion and identify σ_{damper}. The case study shows that, within the degradation range considered in this study, σ_{damper} contributes little relative to a typical $\sigma_{base} \approx 0.6$, indicating that the between-scenario spread remains limited under the adopted scenario settings and demonstrating adequate resolution of the proposed identification even when incremental uncertainty is weak.

(3) Assuming a power-law seismic hazard and lognormal collapse fragility, the annual collapse rate λ_c of viscous-damped structures is expressed in closed form as a function of the median collapse intensity $\hat{S}_c$, total uncertainty $\sigma_{total,damp}$, and hazard parameters (k_0,k). Analytical expressions are derived to back-calculate the minimum median capacity and the acceptable CMR from a target annual collapse probability. While consistent in form with ATC-63/FEMA P-750, the formulation explicitly treats $\sigma_{total,damp}$ as a variable, so acceptable CMR becomes a function of site hazard, target annual risk, and damping-related uncertainty rather than a single system-dependent constant.

(4) In application, the study first converts the FEMA P-750 "50-year collapse probability" target to the annual scale and corresponding acceptable CMR. It then maps CECS 392 rare/very-rare conditional limits to socially acceptable annual collapse probabilities under Chinese hazard and design-spectrum conditions, covering 6–9° intensities, Category B/C buildings, and rare/very-rare levels. Acceptable CMRs are computed on a grid of $\sigma_{total,damp}$ values in [0.50, 0.90], so that the practical influence of plausible baseline uncertainty on the required collapse margin can be read directly rather than inferred from a single point assumption. Compared with prior work, the framework spans a broader set of intensities and importance classes and incorporates very-rare constraints, providing directly usable quantitative criteria for CMR-based, risk-consistent checks in the Chinese code context.

(5) For the case study, acceptable CMR increases monotonically with $\sigma_{total,damp}$ for both building categories at all intensities, with stronger amplification at higher intensity and importance—reflecting uncertainty amplification in collapse performance. However, under a 20% damping-coefficient reduction and 7% partial failure, the incremental contribution of σ_{damper} to $\sigma_{total,damp}$ is limited, yielding acceptable CMRs close to those of conventional structures under the same σ_{base}. For the present case study, this indicates that viscous dampers increase median collapse capacity without materially increasing total dispersion within the degradation range considered in this study; the required safety margins are governed primarily by background uncertainty and site hazard.

Overall, the study establishes a practical workflow for viscous-damped structures: uncertainty stratification → multi-scenario IDA → random-effects identification of (σ_{damper}) → hazard convolution and mapping to socially acceptable annual collapse probability → chart-based acceptable CMR. The present case study supports the transferability of this workflow at the methodological level, because the key inputs of hazard definition, fragility

characterization, and target collapse-risk constraints are explicitly separable and replaceable. Accordingly, the framework supports project-level risk-consistent verification and can, in principle, be extended to more severe degradation, finer scenario partitioning, and larger samples. However, broader transferability across different structural typologies, damper layouts, and hazard datasets should be verified in future studies.

Author Contributions: Conceptualization, X.Z. and W.P.; methodology, X.Z.; software, X.Z.; validation, X.Z. and W.P.; formal analysis, X.Z.; investigation, X.Z.; resources, W.P.; data curation, X.Z.; writing—original draft preparation, X.Z.; writing—review and editing, W.P.; visualization, X.Z.; supervision, W.P.; project administration, W.P. All authors have read and agreed to the published version of the manuscript.

Funding: This research was funded by the National Natural Science Foundation of China, grant number 32060368, and the National Natural Science Foundation of China, grant number 42367025.

Institutional Review Board Statement: Not applicable.

Informed Consent Statement: Not applicable.

Data Availability Statement: The original contributions presented in this study are included in the article. Further inquiries can be directed to the corresponding author.

Conflicts of Interest: The authors declare no conflicts of interest.

References

1. Lan, X.; Wei, G.; Zhang, X. Study on the Influence and Optimization Design of Viscous Damper Parameters on the Damping Efficiency of Frame Shear Wall Structure. *Buildings* **2024**, *14*, 497. [CrossRef]
2. Chalarca, B.; Filiatrault, A.; Perrone, D. Expected Seismic Response and Annual Seismic Loss of Viscously Damped Braced Steel Frames. *Eng. Struct.* **2024**, *303*, 117569. [CrossRef]
3. Scozzese, F.; Gioiella, L.; Dall'Asta, A.; Ragni, L.; Tubaldi, E. Influence of Viscous Dampers Ultimate Capacity on the Seismic Reliability of Building Structures. *Struct. Saf.* **2021**, *91*, 102096. [CrossRef]
4. Zhou, Y.; Xiao, Y.; Sebaq, M.S. Energy-based Fragility Curves of Building Structures Equipped with Viscous Dampers. *Structures* **2022**, *44*, 1660–1679. [CrossRef]
5. FEMA. *Quantification of Building Seismic Performance Factors (FEMA P695)*; Federal Emergency Management Agency: Washington, DC, USA, 2009.
6. Hassanzadeh, A.; Aghakouchak, A.A.; Moghadam, A.S. Seismic collapse safety and risk-targeted evaluation of self-centering steel moment frames with SMA bars. *Earthq. Eng. Struct. Dyn.* **2024**, *53*, 1905–1929. [CrossRef]
7. Zhang, Y.; He, Z. Acceptable values of collapse margin ratio with different confidence levels. *Struct. Saf.* **2020**, *84*, 101938. [CrossRef]
8. Xian, L.; Li, J.; Wang, Z.; Zhang, N. Assessing seismic collapse safety and retrofitting low-ductility RC frame structures on the basis of acceptable collapse safety margin in China. *Appl. Sci.* **2020**, *10*, 1238. [CrossRef]
9. Fazileh, F.; Fathi-Fazl, R.; Dolati, A.; Ventura, C.E.; Saatcioglu, M.; Lau, D.; Yang, T.; Sadeghian, V.; Erochko, J. Methodology for determination of seismic force modification factors in Canada: Performance-based unified procedure. *Earthq. Spectra* **2023**, *39*, 218–241. [CrossRef]
10. Siddiquee, K.N.; Billah, A.M.; Issa, A. Seismic collapse safety and response modification factor of concrete frame buildings reinforced with superelastic shape memory alloy (SMA) rebar. *J. Build. Eng.* **2021**, *42*, 102468. [CrossRef]
11. Akl, A.; El-Tawil, S. Seismic collapse risk assessment of low-aspect-ratio reinforced concrete shear walls using the FEMA P695 methodology. *ASCE Struct. Eng. Mech./Struct. Eng.* **2023**, *149*, 04022237. [CrossRef]
12. Monti, G.; Chioccarelli, E.; Iervolino, I. Towards risk-targeted seismic hazard models for Europe. *Sci. Rep.* **2023**, *13*, 36947. [CrossRef] [PubMed]
13. Mohebi, B.; Asgarian, B.; Jafari, A. Enhancing seismic performance of buckling-restrained braced frames: Collapse risk and mean annual frequency of collapse evaluation. *Innov. Infrastruct. Solut.* **2023**, *23*, 243. [CrossRef]
14. Gallegos, M.F.; Araya-Letelier, G.; Lopez-Garcia, D.; Parra, P.F. Collapse Assessment of Mid-Rise RC Dual Wall-Frame Buildings Subjected to Subduction Earthquakes. *Buildings* **2023**, *13*, 880. [CrossRef]
15. Heshmati, M.; Khatami, A.; Shakib, H. FEMA P695 methodology for safety margin evaluation of steel moment resisting frames subjected to near-field and far-field records. *SN Appl. Sci.* **2021**, *3*, 185. [CrossRef]

16. Zhang, Y.; Ding, Y.; Xu, G. Limit states of impact-buffered viscous dampers: A new model and the implications for the seismic fragility of bridges subjected to near-fault pulse-like ground motions. *Soil Dyn. Earthq. Eng.* **2025**, *195*, 109416. [CrossRef]
17. Qiu, W.; Wen, H.; Gong, C.; Zhang, Z.; Li, W.; Li, S. Seismic Fragility and Loss Assessment of a Multi-Story Steel Frame with Viscous Damper in a Corrosion Environment. *Buildings* **2025**, *15*, 2515. [CrossRef]
18. *CECS 392-2014*; Code for Anti-Collapse Design of Building Structures. China Planning Press: Beijing, China, 2014.
19. *FEMA P-750*; NEHRP Recommended Seismic Provisions for New Buildings and Other Structures. Federal Emergency Management Agency: Washington, DC, USA, 2009.
20. *ASCE/SEI 7-10*; Minimum Design Loads for Buildings and Other Structures. American Society of Civil Engineers: Reston, VA, USA, 2010.

Disclaimer/Publisher's Note: The statements, opinions and data contained in all publications are solely those of the individual author(s) and contributor(s) and not of MDPI and/or the editor(s). MDPI and/or the editor(s) disclaim responsibility for any injury to people or property resulting from any ideas, methods, instructions or products referred to in the content.